Journal of Materials Chemistry A

ROYAL SOCIETY OF CHEMISTRY

PAPER

View Article Online
View Journal | View Issue

Check for updates

Cite this: J. Mater. Chem. A, 2020, 8, 22206

Structure, electrical conductivity and oxygen transport properties of Ruddlesden–Popper phases $Ln_{n+1}Ni_nO_{3n+1}$ (Ln = La, Pr and Nd; n = 1, 2 and 3)†

Jia Song, ‡[a] De Ning,§[b] Bernard Boukamp,[c] Jean-Marc Bassat[d] and Henny J. M. Bouwmeester *[aef]

Received 9th July 2020
Accepted 30th September 2020

DOI: 10.1039/d0ta06731h

rsc.li/materials-a

Layered Ruddlesden–Popper (RP) lanthanide nickelates, $Ln_{n+1}Ni_nO_{3n+1}$ (Ln = La, Pr and Nd; n = 1, 2 and 3), are considered potential cathode materials in solid oxide fuel cells. In this study, the thermal evolution of the structure, oxygen nonstoichiometry, electrical conductivity and oxygen transport properties of $La_2NiO_{4+\delta}$, $Nd_2NiO_{4+\delta}$, $La_3Ni_2O_{7-\delta}$, $La_4Ni_3O_{10-\delta}$, $Pr_4Ni_3O_{10-\delta}$ and $Nd_4Ni_3O_{10-\delta}$ are investigated. Phase transitions involving a disruption of the cooperative tilting of the perovskite layers in the low-temperature structure thereby transforming it to a more symmetric structure are observed in several of the materials upon heating in air. $Pr_4Ni_3O_{10-\delta}$ and $Nd_4Ni_3O_{10-\delta}$ show no phase transition from room temperature up to 1000 °C. High density ceramics (>96%) are obtained after sintering at 1300 °C and (for n = 2 and n = 3 members) post-sintering annealing at reduced temperatures. Data for the electrical conductivity measurements on these specimens indicate itinerant behaviour of the charge carriers in the RP nickelates. The increase in p-type conductivity with the order n of the RP phase is interpreted as arising from the concomitant increase in the formal valence of Ni. The observations can be interpreted in terms of a simple energy band scheme, showing that electron holes are formed in the $\sigma_{x^2-y^2}\uparrow$ band upon increasing the oxidation state of Ni. Electrical conductivity relaxation measurements reveal remarkable similarities between the surface exchange coefficients (k_{chem}) of the different RP phases despite the differences in the order parameter n and the nature of the lanthanide ion. Calculation of the oxygen self-diffusion coefficients (D_s) from the experimental values of the chemical diffusion coefficients (D_{chem}), using the corresponding data of oxygen non-stoichiometry from thermogravimetry measurements, shows that these are strongly determined by the order parameter n. The value of D_s decreases almost one order of magnitude on going from the n = 1 members $La_2NiO_{4+\delta}$ and $Nd_2NiO_{4+\delta}$ to the n = 2 member $La_3Ni_2O_{7-\delta}$, and again one order of magnitude on going to the n = 3 members $La_4Ni_3O_{10-\delta}$, $Pr_4Ni_3O_{10-\delta}$ and $Nd_4Ni_3O_{10-\delta}$. The results confirm that oxygen-ion transport in the investigated RP nickelates predominantly occurs *via* an interstitialcy mechanism within the rock-salt layer of the structures.

1. Introduction

Layered Ruddlesden–Popper (RP) nickelates with the generic formula $(LnNiO_3)_nLnO$ (Ln = La, Pr, Nd; n = 1, 2, 3) have attracted considerable interest for potential application as the cathode for intermediate-temperature solid oxide fuel cells (IT-SOFCs).[1–7] Their crystal structures can be viewed as a stack of one rock-salt LnO layer with a finite number (n) of perovskite-type $LnNiO_3$ layers along the principal crystallographic axis.

[a]Electrochemistry Research Group, Membrane Science and Technology, MESA+ Institute for Nanotechnology, University of Twente, P.O. Box 217, 7500 AE, Enschede, The Netherlands. E-mail: h.j.m.bouwmeester@utwente.nl

[b]Helmholtz-Zentrum Berlin für Materialien und Energie, Hahn-Meitner-Platz 1, 14109 Berlin, Germany

[c]Inorganic Materials Science, MESA+ Institute for Nanotechnology, University of Twente, P.O. Box 217, 7500 AE, Enschede, The Netherlands

[d]CNRS, Université de Bordeaux, Institut de Chimie de la Matière Condensée de Bordeaux (ICMCB), 87 Av. Dr Schweitzer, F-33608 Pessac Cedex, France

[e]CAS Key Laboratory of Materials for Energy Conversion, Department of Materials Science and Engineering, University of Science and Technology of China, Hefei, 230026, P. R. China

[f]Forschungszentrum Jülich GmbH, Institute of Energy and Climate Research-IEK-1, Leo-Brandt-Str. 1, D-52425, Jülich, Germany

† Electronic supplementary information (ESI) available. See DOI: 10.1039/d0ta06731h

‡ Separation and Conversion Technology, Flemish Institute for Technological Research (VITO), Boeretang 200, Mol 2400, Belgium.

§ Center for Information Photonics and Energy Materials, Shenzhen Institutes of Advanced Technology, Chinese Academy of Sciences, Shenzhen 518055, P. R. China.

The $n = 1$ members with composition $Ln_2NiO_{4+\delta}$ adopt the K_2NiF_4-type structure.[8–13] A high concentration of interstitial oxygen is found in the rock-salt layers, which accounts for the highly anisotropic and fast diffusion of oxygen.[14–17] The migration of oxygen in the crystal proceeds *via* an interstitialcy (or push pull) mechanism, whereby the oxygen vacancy formed at an apical site by the movement of apical oxygen to an interstitial site is filled by a nearby interstitial oxygen.[17–19] Excellent thermal stability is found for $La_2NiO_{4+\delta}$ and $Nd_2NiO_{4+\delta}$ up to 1400 °C in air.[20] SOFCs with cathode materials of $La_2NiO_{4+\delta}$ and $Nd_2NiO_{4+\delta}$ show no degradation in cell performance after hundreds of hours of operation at 750–800 °C.[21,22] $Pr_2NiO_{4+\delta}$, on the other hand, starts to decompose upon annealing in air above 580 °C to a mixture consisting of $Pr_4Ni_3O_{10-\delta}$, $PrNiO_{3-\delta}$ and Pr_6O_{11}.[23–31] Though apparent oxygen diffusion and surface exchange kinetics are enhanced after thermal decomposition,[23] a significant degradation of cell performance is observed for the SOFC with $Pr_2NiO_{4+\delta}$ as the cathode after 1000 h of operation at 750 °C.[22]

Meanwhile, there is a growing interest in using higher order RP nickelates as the cathode material. Among the $n = 2$ members, $Ln_3Ni_2O_{7-\delta}$ (Ln = La, Pr, Nd), so far only $La_3Ni_2O_{7-\delta}$ could be prepared in a phase-pure form, while $Pr_3Ni_2O_{7-\delta}$ and $Nd_3Ni_2O_{7-\delta}$ have been observed only as disordered intergrowths in the corresponding $n = 3$ members.[32] Several studies have investigated the electrode performance of RP-type lanthanum nickelates with controversial results. Using impedance spectroscopy on symmetric cells with $La_{0.9}Sr_{0.1}Ga_{0.8}Mg_{0.2}O_{3-\delta}$ as the electrolyte, Amow *et al.*[33] found that the area-specific resistance (ASR) in the temperature range 500–900 °C followed the trend $La_4Ni_3O_{10-\delta} < La_3Ni_2O_{7-\delta} < La_2NiO_{4+\delta}$. This trend is consistent with that of the cell performance of $La_{n+1}Ni_nO_{3n+1}$/SDC/Ni-SDC cell configurations.[13] However, such a trend was not observed in a comparative study on symmetric cells by Woolley *et al.*[34] Sharma *et al.*[3] showed that $La_3Ni_2O_{7-\delta}$ would be a better cathode material than $La_4Ni_3O_{10-\delta}$ based on ASR data of symmetric cells using GCO ($Ce_{0.9}Gd_{0.1}O_{2-\delta}$) as the electrolyte. Increasing the order n of the RP nickelates promotes electrical conductivity and long-term stability in the range 600–800 °C.[4,13,33,35] Apart from material composition, the microstructure of the cathodes is found to play a key role in their performance.[4,36]

In this work, the structure, oxygen nonstoichiometry, electrical conductivity and oxygen transport of $Ln_{n+1}Ni_nO_{3n+1}$ (Ln = La, Pr and Nd; $n = 1$, 2 and 3) are studied. Data on oxygen self-diffusion coefficients and ionic conductivities of $La_3Ni_2O_{7-\delta}$, $La_4Ni_3O_{10-\delta}$, $Pr_4Ni_3O_{10-\delta}$ and $Nd_4Ni_3O_{10-\delta}$ are reported for the first time. $Pr_2NiO_{4+\delta}$, $Pr_3Ni_2O_{7-\delta}$ and $Nd_3Ni_2O_{7-\delta}$ are excluded from this work as the latter two compositions could not be prepared in a phase-pure form, while $Pr_2NiO_{4+\delta}$ fully decomposes after annealing in air above 580 °C, as alluded to above.

2. Experimental

2.1 Sample preparation

Powders of $Ln_{n+1}Ni_nO_{3n+1}$ (Ln = La, Pr, Nd, $n = 1$, 2, 3) were prepared *via* a modified Pechini method as described elsewhere.[37] Stoichiometric amounts of $La(NO_3)_3 \cdot 6H_2O$ (Alfa Aesar, 99.9%), $Pr(NO_3)_3 \cdot 6H_2O$ (Sigma-Aldrich, 99.9%), $Nd(NO_3)_3 \cdot 6H_2O$ (Sigma-Aldrich, 99.9%) and $Ni(NO_3)_2 \cdot 6H_2O$ (Sigma-Aldrich, 99.0–102.0%) were dissolved in water followed by the addition of $C_{10}H_{16}N_2O_8$ (EDTA, Sigma-Aldrich, >99%) and $C_6H_8O_7$ (citric acid, Alfa Aesar, >99.5%) as chelating agents. The pH of the solution was adjusted to 7 using $NH_3 \cdot H_2O$ solution (Sigma-Aldrich, 30 w/v%). After evaporating the water, the foam-like gel reached self-ignition at around 350 °C. The obtained raw powders were ground to fine powders and calcined under various conditions as shown in Table 1. The heating and cooling rates were 2 °C min^{-1}. The obtained phase-pure powders were first ball-milled in ethanol using 2 mm ZrO_2 balls for 2 days to enhance their sinterability before they were pelletized by uniaxial pressing at 25 MPa. Isostatic pressing of pellets was performed at 400 MPa for 2 min. All pellets were sintered at 1300 °C for 4 h in air, while a post-sintering annealing treatment was applied for $La_3Ni_2O_{7-\delta}$, $La_4Ni_3O_{10-\delta}$, $Pr_4Ni_3O_{10-\delta}$ and $Nd_4Ni_3O_{10-\delta}$ under the conditions listed in Table 1. The relative density of the pellets obtained was above 96% of their theoretical value as measured by Archimedes' method. The results were cross-checked by simple calculations based on the weight and geometric volume of the pellets.

Table 1 Calcination, sintering and post-sintering annealing conditions (*i.e.*, temperature, duration and atmosphere) for the different RP nickelates investigated in this study

	Calcination	Sintering	Post-sintering annealing
$La_2NiO_{4+\delta}$	1100 °C 4 h in air	1300 °C 4 h in air	—
$Nd_2NiO_{4+\delta}$	1100 °C 4 h in air	1300 °C 4 h in air	—
$La_3Ni_2O_{7-\delta}$	1150 °C 144 h in air	1300 °C 4 h in air	1100 °C 130 h in air
$La_4Ni_3O_{10-\delta}$	1050 °C 132 h in air	1300 °C 4 h in air	1050 °C 230 h in air
$Pr_4Ni_3O_{10-\delta}$	1000 °C 125 h in pure O_2	1300 °C 4 h in air	1000 °C 110 h in pure O_2
$Nd_4Ni_3O_{10-\delta}$	1000 °C 125 h in pure O_2	1300 °C 4 h in air	1000 °C 170 h in pure O_2

2.2 Phase analysis and surface morphology

The phase purity and crystal structure of the prepared powders and annealed dense pellets were studied by X-ray diffraction (XRD, D2 PHASER, Bruker) with Cu Kα_1 radiation ($\lambda = 1.54060$ Å) in air. The surfaces of the annealed pellets were polished. Data were collected using the step-scan mode in the 2θ range of 20–80° with an increment of 0.01° and a counting time of 5 s. The thermal evolution of the structures was investigated *in situ* using HT-XRD (D8 Advance, Bruker) from 40 °C to 1000 °C with steps of 50–60 °C below 300 °C and steps of 25 °C at higher temperatures. The sample was heated to the desired temperature with a heating rate of 25 °C min^{-1}. After a dwell time of 15 min, the HT-XRD patterns were recorded in the 2θ range of 20–90° with a step size of 0.015° and a counting time of 1.3 s. The FullProf software package was used for Rietveld refinements of the XRD patterns.[38] Scanning electron microscopy (SEM) measurements were performed using a JEOL JSM-6010LA

microscope, operated at a 5 keV accelerating voltage. The SEM images of the polished samples were recorded after thermal etching at 1000 °C for 2 h in air.

2.3 Thermogravimetric analysis

Data of oxygen stoichiometry were collected by thermogravimetric analysis (TGA) of the powders in the pO_2 range of 0.045–0.90 atm between 700 °C and 900 °C with intervals of 25 °C, using a Netzsch STA F3 Jupiter. Measurements were conducted using 2000–3000 mg of powder. Data were collected at 4.5, 10, 21, 42, and 90% O_2 in N_2, which correspond to values of the pO_2 of the gas streams used in the electrical conductivity relaxation (ECR) experiments. The heating and cooling rates were 5 °C min^{-1} and 3 °C min^{-1}, respectively. At the end of each TGA experiment, the powder was held at 100 °C in synthetic air for 3 h. Approximately 30 mg of the powder was subsequently transferred to a Mettler Toledo 851e TGA system to determine the absolute oxygen stoichiometry of the sample by thermal reduction in hydrogen (16% H_2/Ar).

2.4 Electrical conductivity relaxation

Samples for ECR measurements were prepared by grinding and cutting the obtained dense pellets to planar-sheet-shaped sample bars with approximate dimensions of 12 × 5 × 0.5 mm^3. The sample surfaces were polished down to 0.5 μm using diamond polishing discs (JZ Primo, Xinhui China). A four-probe DC method was used to collect data on electrical conductivity. Two gold wires (Alfa Aesar, 99.999%, ∅ = 0.25 mm) were wrapped around the ends of the sample bar for current supply. Two additional gold wires were wrapped 1 mm away from the current electrodes to act as the voltage probes. To ensure good contact between the gold wires and the sample, sulfur-free gold paste (home-made) was applied to the gaps between the sample surface and the gold wires. Finally, the sample was annealed at 950 °C in air for 1 h to sinter the gold paste and to thermally cure the polished sample surface.

The sample was mounted on a holder and placed in an alumina sample containment chamber (or reactor). Two gas streams, each of which had a flow rate of 280 ml min^{-1}, with a different pO_2 were created by mixing dried oxygen and nitrogen in the desired ratios using Brooks GF040 mass flow controllers. A pneumatically operated four-way valve was used to instantaneously switch between both gas streams so that one of them was fed through the reactor. Data on the transient electrical conductivity was collected following oxidation and reduction step changes in pO_2 between 0.10 and 0.21 atm. Measurements were conducted following stepwise cooling from 900 °C to 650 °C with intervals of 25 °C, heating/cooling rates of 10 °C min^{-1} and a dwell time of 60 min at each temperature before data acquisition.

The transient conductivity after each pO_2 step change was normalized according to eqn (1) and fitted to eqn (2)–(4) to obtain the chemical diffusion coefficient D_{chem} and the surface exchange coefficient k_{chem}.

$$g(t) = \frac{\sigma(t) - \sigma_0}{\sigma_\infty - \sigma_0} \quad (1)$$

$$g(t) = 1 - \prod_{i=y,z} \sum_{m=1}^{\infty} \frac{2{L_i}^2}{{\beta_{m,i}}^2\left({\beta_{m,i}}^2 + {L_i}^2 + L_i\right)} \frac{\tau_{m,i}}{\tau_{m,i} - \tau_f}\left(e^{-\frac{t}{\tau_{m,i}}} - \frac{\tau_f}{\tau_{m,i}}\left(e^{-\frac{t}{\tau_f}}\right)\right) \quad (2)$$

$$\tau_{m,i} = \frac{{b_i}^2}{D_{chem}{\beta_{m,i}}^2} \quad (3)$$

$$L_i = \frac{b_i}{L_c} = \beta_{m,i} \tan \beta_{m,i} \quad (4)$$

In these equations, $g(t)$ is the normalized conductivity, σ_0 and σ_∞ are the conductivities $\sigma(t)$ at time $t = 0$ and $t = \infty$, respectively, τ_f is the flush time, and $2b_i$ is the sample dimension along coordinate i, whilst the values of $\beta_{m,i}$ are the non-zero roots of eqn (4). $L_c = D_{chem}/k_{chem}$ is the critical thickness below which oxygen surface exchange prevails over bulk oxygen diffusion in determining the rate of re-equilibration after a pO_2 step change. The flush time τ_f was calculated from

$$\tau_f = \frac{V_r}{\theta_v}\frac{T_{STP}}{T_r} \quad (5)$$

which assumes perfect mixing of the gas in the sample containment chamber. In eqn (5), V_r is the corresponding volume, θ_v is the gas flow rate through the chamber, T_r is the temperature inside the chamber, and T_{STP} is the temperature under standard conditions. The small chamber volume (2.58 cm^3) and the high gas flow rate (280 ml min^{-1}) ensured a flush time between 0.13 s at 900 °C and 0.16 s at 650 °C. Curve fitting of the normalized transient conductivity was performed using a non-linear least-squares program based on the Levenberg–Marquardt algorithm. More detailed descriptions of the ECR technique and the model used for data fitting are given elsewhere.[39,40]

3. Results and discussion

3.1 Synthesis and consolidation

The calcination, sintering and post-sintering annealing conditions of the different RP nickelates investigated in this work are compiled in Table 1. The powders obtained were calcined in air apart from the powders of $Pr_4Ni_3O_{10-\delta}$ and $Nd_4Ni_3O_{10-\delta}$, which could only be prepared in a phase-pure form by calcination at 1000 °C under flowing oxygen. The latter is considered consistent with observations by Vibhu *et al.*[4] Using thermogravimetric analysis, these authors showed decomposition of $Pr_4Ni_3O_{10-\delta}$ into $Pr_2NiO_{2+\delta}$ and NiO upon heating (2 °C min^{-1}) under air above 1050 °C, but above 1120 °C when these experiments were conducted under oxygen. Note from Table 1 that long annealing times (125–144 h) are required for the $n = 2$ and $n = 3$ RP nickelates to obtain phase-pure powders.

A sintering temperature of 1300 °C was found necessary to sinter pressed powder compacts of the RP nickelates to high density (>96%). It should be noted that this temperature is well above the reported decomposition temperatures of the $n = 2$

and $n = 3$ members $La_3Ni_2O_{7-\delta}$, $La_4Ni_3O_{10-\delta}$, $Pr_4Ni_3O_{10-\delta}$ and $Nd_4Ni_3O_{10-\delta}$.[4,35,41,42] The cited studies demonstrated that decomposition into the $n = 1$ member (and NiO) occurs which, as expected, has improved sintering behaviour over the $n = 2$ and $n = 3$ members. In an attempt to regain the pure phases of $La_3Ni_2O_{7-\delta}$, $La_4Ni_3O_{10-\delta}$, $Pr_4Ni_3O_{10-\delta}$ and $Nd_4Ni_3O_{10-\delta}$, a post-sintering annealing step was performed at a lower temperature, as indicated in Table 1. Annealing times between 110 and 230 h were necessary to obtain almost single-phase materials. The phase purity of the samples obtained after post-sintering annealing was studied by XRD, which is discussed in the next section.

3.2 Crystal structure and phase transitions

Fig. 1 shows the results of Rietveld refinements of the room-temperature XRD patterns of the prepared powders. All compositions appear to be single-phase as no diffraction peaks of impurity phases can be detected. The refined values of the lattice parameters and reliability factors for the different compositions are given in Table 2. The cell parameters for all compositions are in good agreement with those reported previously in the literature.[5,10,41,43–47] The crystallographic parameters obtained from the Rietveld refinements are listed in Table S1.† The corresponding structures of the RP nickelates are shown in Fig. 2.

The X-ray diffractograms of $La_2NiO_{4+\delta}$ and $Nd_2NiO_{4+\delta}$ can be fitted in the orthorhombic space group *Fmmm*, which is in good agreement with previous analyses of data from synchrotron X-ray powder diffraction (SXRPD) and neutron powder diffraction (NPD) of both materials.[10,44,45] The XRD pattern of $La_3Ni_2O_{7-\delta}$ can be fitted in the orthorhombic space group *Cmmm*, consistent with the results from Mössbauer spectroscopy and XRD by Kiselev *et al.*[46] The XRD patterns of the $n = 3$ RP

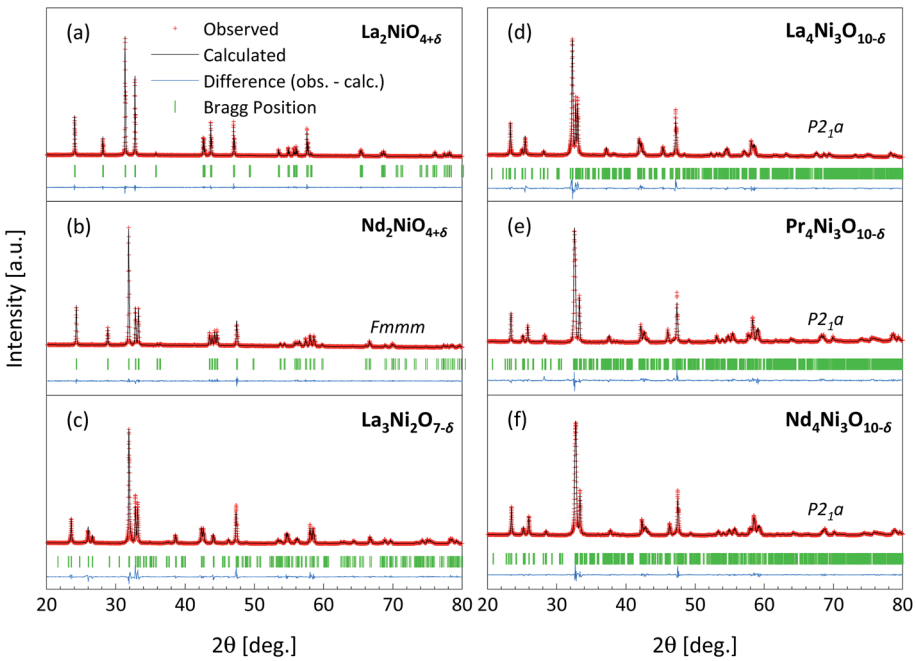

Fig. 1 Rietveld refinements (black lines) of the room temperature XRD powder patterns (red crosses) for (a) $La_2NiO_{4+\delta}$ (*Fmmm*), (b) $Nd_2NiO_{4+\delta}$ (*Fmmm*), (c) $La_3Ni_2O_{7-\delta}$ (*Cmmm*), (d) $La_4Ni_3O_{10-\delta}$ ($P2_1a$), (e) $Pr_4Ni_3O_{10-\delta}$ ($P2_1a$), and (f) $Nd_4Ni_3O_{10-\delta}$ ($P2_1a$). Also shown are the Bragg positions (green vertical bars) and the differences between the calculated and observed patterns (blue lines).

Table 2 Lattice parameters and reliability factors obtained from Rietveld refinements of the room temperature XRD patterns

	$La_2NiO_{4+\delta}$	$Nd_2NiO_{4+\delta}$	$La_3Ni_2O_{7-\delta}$	$La_4Ni_3O_{10-\delta}$	$Pr_4Ni_3O_{10-\delta}$	$Nd_4Ni_3O_{10-\delta}$
Space group	*Fmmm*	*Fmmm*	*Cmmm*	$P2_1a$	$P2_1a$	$P2_1a$
a/Å	5.4608(7)	5.44647(7)	5.39431(5)	5.4160(1)	5.37556(5)	5.36373(5)
b/Å	5.4612(7)	5.377711(7)	5.45002(6)	5.4656(1)	5.46462(6)	5.45221(7)
c/Å	12.67758(8)	12.36233(18)	20.5264(2)	27.9750(6)	27.5463(3)	27.4100(3)
β/°	90	90	90	90.179(1)	90.283(1)	90.292(1)
V/Å^3	378.098(2)	362.0475(4)	603.4595(3)	828.112(1)	809.1756(5)	801.5767(4)
R_{wp}/%	13.9	11.8	18.1	14.7	12.6	11.0
R_{exp}/%	11.7	8.28	8.77	5.87	7.04	4.48
R_{Bragg}/%	2.37	2.96	7.39	6.57	5.14	3.19
χ^2	1.942	2.025	4.259	6.271	3.203	6.338

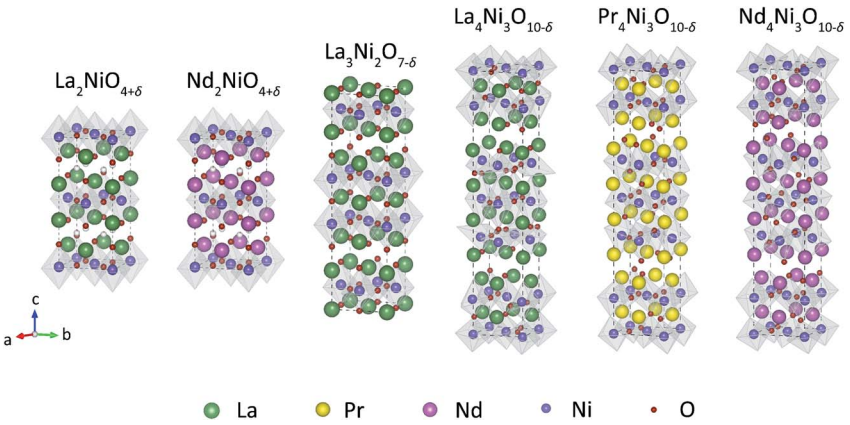

Fig. 2 Unit cells of RP phases $Ln_{n+1}Ni_nO_{3n+1}$ (Ln = La, Pr, Nd; n = 1, 2, 3) obtained from Rietveld refinements of the room temperature XRD powder patterns.

nickelates were fitted using the monoclinic space group $P2_1a$, which is in agreement with the results from high-resolution SXRPD and NPD.[5,41,43,47] The lattice parameters of the $n = 3$ members are found to increase in the order $Nd_4Ni_3O_{10-\delta}$ < $Pr_4Ni_3O_{10-\delta}$ < $La_4Ni_3O_{10-\delta}$. The corresponding crystal structures become more distorted in the reverse order as can be derived from the value of the monoclinic angle (β) obtained from the refinements. The degree of structural distortion can be linked to the size of the lanthanide ion.[32,48,49]

Fig. 3 shows the HT-XRD pattern of $Pr_4Ni_3O_{10-\delta}$ recorded in air from 40 °C to 1000 °C. The patterns for the other compositions investigated in this work are shown in Fig. S1–S5.† All compositions are found to be phase-pure, *i.e.*, no impurity peaks are observed up to 1000 °C. Fig. 4 shows the lattice parameters obtained from refinement of the HT-XRD patterns. The thermal evolution of the structure of the RP nickelates is discussed below. In several of these, a phase transition is observed, driven by a disruption of the cooperative tilting of the NiO_6 octahedra in the low-temperature structure transforming it to a more symmetric structure at elevated temperature.[50] It should be noted that the appearance of the phase transition may be influenced by the degree of oxygen nonstoichiometry of the material under the conditions of the experiment.[51,52]

$n = 1$ RP nickelates

$La_2NiO_{4+\delta}$ shows a phase transition from orthorhombic (*Fmmm*) to tetragonal (*F*4/*mmm*) at approximately 175 °C, as can be derived from the data in Fig. 4a. This result is consistent with that found by *in situ* high-temperature NPD measurements.[10,53] Due to the relatively small orthorhombic distortion (approximately 0.1% difference between cell parameters a and b), the separation between the orthorhombic (2 0 0) and (0 2 0) peaks is hardly noticeable (see the inset of Fig. S1†).

The Rietveld refinements of the HT-XRD patterns of $Nd_2NiO_{4+\delta}$ (Fig. 4b) reveal a phase transition from orthorhombic (*Fmmm*) to tetragonal (*F*4/*mmm*) at around 550 °C. This temperature is about 50 °C lower than that evaluated for $Nd_2NiO_{4+\delta}$ by means of HT-XRD by Toyosumi *et al.*[52]

$n = 2$ RP nickelates

For $La_3Ni_2O_{7-\delta}$, a gradual merging of the peaks at around 33° is observed with increasing temperature from 300 °C to

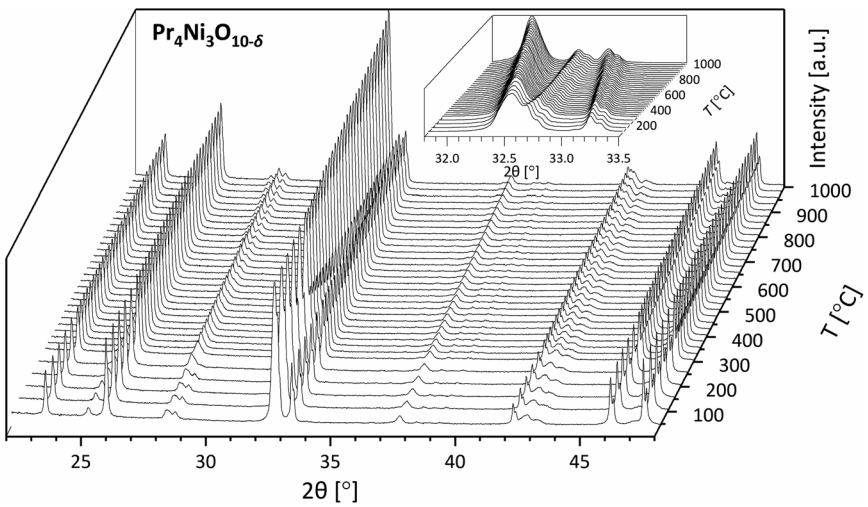

Fig. 3 *In situ* HT-XRD patterns of $Pr_4Ni_3O_{10-\delta}$ (powder) between 22° and 48° recorded in air from 40 °C to 1000 °C. The inset shows the magnification of the peaks between 31.8–33.5°.

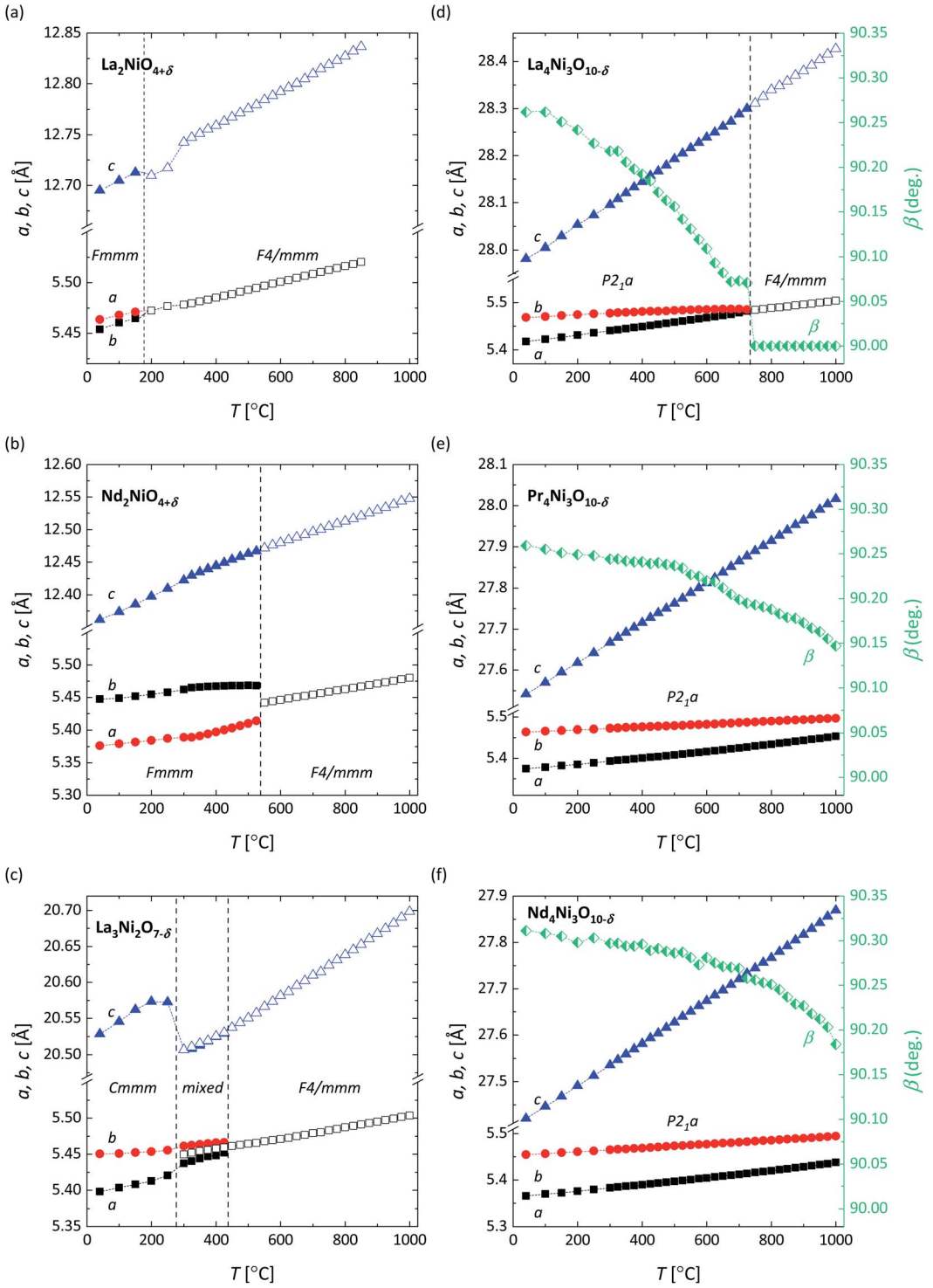

Fig. 4 Lattice parameters (*a*, *b*, *c*) of (a) $La_2NiO_{4+\delta}$, (b) $Nd_2NiO_{4+\delta}$, (c) $La_3Ni_2O_{7-\delta}$, (d) $La_4Ni_3O_{10-\delta}$, (e) $Pr_4Ni_3O_{10-\delta}$ and (f) $Nd_4Ni_3O_{10-\delta}$ as a function of temperature. (d), (e) and (f) also show the temperature dependence of the angle β in the structure.

450 °C (Fig. S3†), suggesting a phase transition in this temperature range. The HT-XRD patterns of the high-temperature phase of $La_3Ni_2O_{7-\delta}$ can be well-fitted using the tetragonal space group *F*4/*mmm*. The results of the Rietveld refinements of the HT-XRD patterns in Fig. 4c confirm an orthorhombic (*Cmmm*) to tetragonal (*F*4/*mmm*) phase transition at around 300 °C. A mixture of *Cmmm* and *F*4/*mmm* phases is found between 300 °C and 450 °C. The refined weight percentages of the two phases at different temperatures are listed in Table 3.

$n = 3$ RP nickelates

The results of the refinements of the HT-XRD patterns of $La_4Ni_3O_{10-\delta}$ reveal a phase transition from monoclinic ($P2_1a$) to tetragonal (*F*4/*mmm*) at around 750 °C, as shown in Fig. 4d. The

Table 3 Weight percentages of *Cmmm* and *F4/mmm* phases at different temperatures in $La_3Ni_2O_{7-\delta}$ from Rietveld refinements of the HT-XRD data

Wt%	300 °C	325 °C	350 °C	375 °C	400 °C	425 °C	450 °C
Cmmm	97.75	97.28	97.05	53.77	40.73	19.16	7.64
F4/mmm	2.25	2.72	2.95	46.23	59.27	80.84	92.36

observed phase transition temperature is found to be in good agreement with that reported by Nagell *et al.*[43]

The HT-XRD patterns of $Pr_4Ni_3O_{10-\delta}$ in Fig. 3 show no phase transition in the experimental temperature region. The (2 0 0) and (0 2 0) peaks approach each other up to the highest temperature of the measurements, confirming that the structure of $Pr_4Ni_3O_{10-\delta}$ remains monoclinic ($P2_1a$) up to 1000 °C. The refined monoclinic angle decreases from 99.25° at 40 °C to 90.15° at 1000 °C, as shown in Fig. 4e.

Similar to $Pr_4Ni_3O_{10-\delta}$, the crystal structure of $Nd_4Ni_3O_{10-\delta}$ appears to be monoclinic ($P2_1a$) in the temperature range 40–1000 °C. The corresponding results of the refinements of the HT-XRD patterns are shown in Fig. 4f.

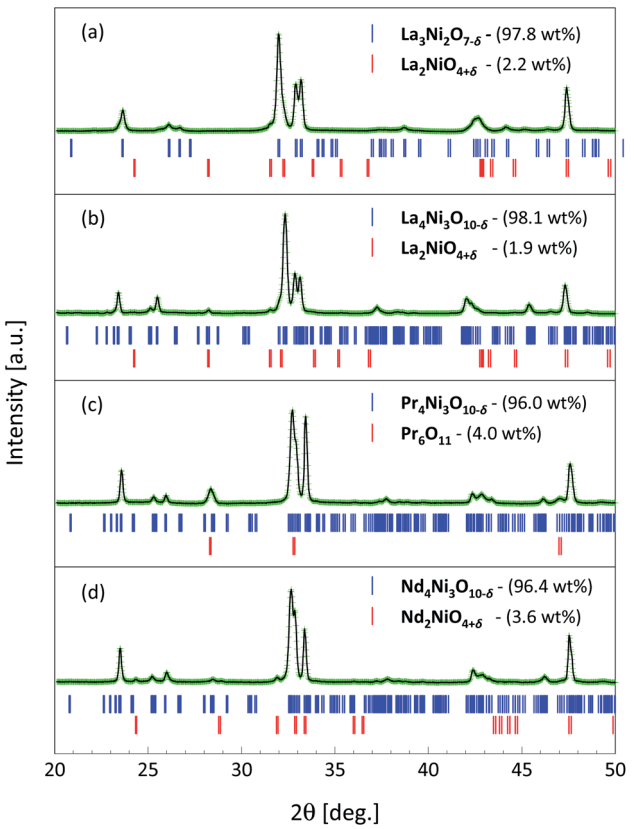

Fig. 5 Rietveld refinements (green crosses) of the room temperature X-ray diffractograms (black lines) of polished dense pellets of (a) $La_3Ni_2O_{7-\delta}$, (b) $La_4Ni_3O_{10-\delta}$, (c) $Pr_4Ni_3O_{10-\delta}$, and (d) $Nd_4Ni_3O_{10-\delta}$ after post-sintering annealing (*cf.* Table 1). Minor impurities are found in the pellets and their refined weight percentages are indicated in brackets. Bragg positions of the main phases and impurities are indicated as vertical bars.

The phase purity of the sintered samples was analyzed by XRD. No impurities were found in samples $La_2NiO_{4+\delta}$ and $Nd_2NiO_{4+\delta}$. The XRD patterns of consolidated samples $La_3Ni_2O_{7-\delta}$, $La_4Ni_3O_{10-\delta}$, $Pr_4Ni_3O_{10-\delta}$ and $Nd_4Ni_3O_{10-\delta}$ obtained after post-sintering annealing are shown in Fig. 5. Rietveld refinements confirm the presence of minor impurities in these samples. The corresponding results are listed in Table S2.† As discussed above, the presence of impurities in these samples is assigned to (partial) thermal decomposition at the applied sintering temperatures (*cf.* Table 1). Over 96 wt% of the main phase is obtained after post-sintering annealing. More specifically, 2.2 wt% of the $n = 1$ RP phase is found to be an impurity in the sintered pellet of $La_3Ni_2O_{7-\delta}$, 1.9 wt% in that of $La_4Ni_3O_{10-\delta}$ and 3.6 wt% in that of $Nd_4Ni_3O_{10-\delta}$. 4.0 wt% of the Pr_6O_{11} impurity is found in the $Pr_4Ni_3O_{10-\delta}$ pellet. No evidence of NiO is found in the diffractograms, despite the stoichiometric ratio for the $n = 2$ and $n = 3$ RP nickelates suggesting the formation of NiO as the by-product of the decomposition reaction into the $n = 1$ member during sintering at 1300 °C. The absence of NiO in the samples after subsequent post-sintering annealing to reform the higher-order RP phase may be due either to volatility of NiO[54–56] or its weaker contribution to scattering compared with rare-earth oxides. In none of the sintered samples was evidence found for a preferred orientation (*i.e.*, crystallographic texture), suggesting that grains in the sintered materials are randomly oriented. Furthermore, to the best of our knowledge, this is the first report of sintered bodies of the above-mentioned $n = 2$ and $n = 3$ RP nickelates with such a high purity (>96 wt%) and high density (>96%).

3.3 Oxygen nonstoichiometry

Fig. 6 shows the data of TGA measurements of $Nd_2NiO_{4+\delta}$ under a reducing atmosphere. Similar data were obtained for $La_2NiO_{4+\delta}$, $La_4Ni_3O_{10-\delta}$, $Pr_4Ni_3O_{10-\delta}$ and $Nd_4Ni_3O_{10-\delta}$ and are presented in Fig. S6–S9.† In agreement with the literature reports, a two-step reduction process is found for all compositions.[4,32,57–59] The final decomposition products are assumed to

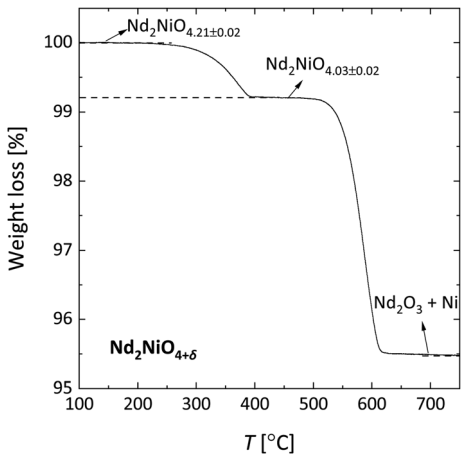

Fig. 6 TGA weight loss curve recorded for $Nd_2NiO_{4+\delta}$ in 16% H_2/Ar. The oxygen nonstoichiometries as indicated were calculated using the oxide reduced to Nd_2O_3 and Ni as the reference state.

Table 4 Oxygen nonstoichiometry (δ) of RP nickelates obtained after cooling in air to room temperature and comparison with the literature data

	$La_2NiO_{4+\delta}$	$Nd_2NiO_{4+\delta}$	$La_3Ni_2O_{7-\delta}$	$La_4Ni_3O_{10-\delta}$	$Pr_4Ni_3O_{10-\delta}$	$Nd_4Ni_3O_{10-\delta}$
This study	0.16 ± 0.01	0.21 ± 0.02	—	0.15 ± 0.04	0.21 ± 0.03	0.22 ± 0.03
	0.15 ± 0.01	0.20 ± 0.01	0.08	0.13	0.15 ± 0.03*	0.15 ± 0.03*
Ref.		8 and 51	62	63	32	41

be Ln_2O_3 and Ni. The decomposition reaction can thus be represented as

$$Ln_{n+1}Ni_nO_{3n+1\pm\delta} \rightarrow \frac{n+1}{2}Ln_2O_3 + nNi + \frac{3n-1\pm2\delta}{4}O_2 \quad (6)$$

The initial (*i.e.*, room temperature) oxygen nonstoichiometries calculated using the oxide reduced in 16% H_2/Ar as the reference state are listed in Table 4. It should be noted that, in general, the oxygen stoichiometry may be influenced by the thermal history of the powder. Note further from Table 4 that oxygen hyper-stoichiometry is found for $La_2NiO_{4+\delta}$ and $Nd_2NiO_{4+\delta}$, while oxygen hypo-stoichiometry is found for all other investigated compositions.

Good agreement is obtained between the value of δ for $La_4Ni_3O_{10-\delta}$ and that evaluated from the data of near-edge X-ray absorption spectroscopy (XANES).[60] Somewhat larger values of δ are found for $Pr_4Ni_3O_{10-\delta}$ and $Nd_4Ni_3O_{10-\delta}$ in this study when compared to the corresponding values reported for oxygen-cooled samples.[32,41]

The pO_2 dependence of the oxygen nonstoichiometry was investigated in the range of 0.045–0.900 atm at temperatures of 700–900 °C. The corresponding data are shown in Fig. 7. The corresponding weight loss curves are presented in Fig. S10–S14.† Excellent agreement with the literature data is found for $La_2NiO_{4+\delta}$ and $Nd_2NiO_{4+\delta}$,[61,62] as demonstrated in Fig. S15.†

3.4 Electrical conductivity

Arrhenius plots of the electrical conductivity (σ_{el}) of the investigated RP $Ln_{n+1}Ni_nO_{3n+1}$ nickelates, measured in air in the range 650–900 °C, are shown in Fig. 8a. As illustrated in this figure, excellent agreement is obtained with the published data for $La_2NiO_{4+\delta}$ and $Nd_2NiO_{4+\delta}$.[12,63] For $La_3Ni_2O_{7-\delta}$, $La_4Ni_3O_{10-\delta}$, $Pr_4Ni_3O_{10-\delta}$ and $Nd_4Ni_3O_{10-\delta}$, however, noticeably higher values of σ_{el} are found compared with those reported in the literature.[4,33,64,65] A comparison of the data from this study with the corresponding data from the literature, at 750 °C in air, is shown in Table S3.† The observed discrepancies can be ascribed, in part, to small differences in composition (*e.g.* impurities), but more likely to the much higher densities (>96%) of the samples used in the present study when compared with those used in the cited studies (*cf.* Table S3†). Fig. 8b shows the pO_2 dependence of σ_{el}, at 900 °C, in the range of 0.01–1 atm. For all the investigated compositions, σ_{el} is found to decrease with decreasing pO_2, which on the log scale is the most pronounced for the $n = 1$ RP phases $La_2NiO_{4+\delta}$ and $Nd_2NiO_{4+\delta}$, exhibiting the lowest conductivities. Note further from Fig. 8a and b that within the range of temperature and oxygen partial pressure, σ_{el} of $Ln_{n+1}Ni_nO_{3n+1}$ increases with the order n.

$La_2NiO_{4+\delta}$ and $Nd_2NiO_{4+\delta}$ are typical p-type conductors as confirmed by their positive Seebeck coefficients in a wide range of temperature.[12,66] Their electrical conductivities display a broad maximum in the range 400–450 °C without discontinuous changes in the Seebeck coefficients, which is frequently interpreted in terms of a metal–semiconductor transition.[12,66] This interpretation has been contested by several authors as the loss in oxygen occurring at elevated temperature brings about a concomitant decrease in the charge carrier density.[67,68]

The strongly correlated charge carriers in the RP nickelates and related transition metal oxides may be viewed as intermediate between localized and delocalized. Goodenough *et al.*[69,70] proposed the coexistence of localized and itinerant electrons in $La_2NiO_{4+\delta}$. The bonding orbitals with ε_g ($d_{x^2-y^2}$,d_{z^2}) symmetry are assumed to be split by the tetragonal distortion into a localized σ_{z^2} orbital and a more delocalized $\sigma_{x^2-y^2}$ band. Electron–electron correlation leads to further splitting of these into low and high spin states, which is more profound for the narrow σ_{z^2} orbitals and less for the $\sigma_{x^2-y^2}$ and the lower energy π_{t2g} (derived from d_{xy},d_{xz},d_{yz}) bands, as schematically shown in Fig. 9. Nakamura *et al.*[12,66] used this band scheme to account for the electrical transport properties of $La_{2-x}Sr_xNiO_{4+\delta}$ (x = 0, 0.2, 0.4) and $Nd_{2-x}Sr_xNiO_{4+\delta}$ (x = 0, 0.2 0.4). The electrical conductivity is found to increase significantly upon partial substitution of La with Sr. Semi-quantitative analysis of the data of oxygen nonstoichiometry, electrical conductivity and Seebeck coefficients supports the itinerant behavior of the electrons at high temperature in both series. A similar band scheme has been proposed to interpret the data of electrical conductivity and magnetic susceptibility of $La_3Ni_2O_{7-\delta}$ (ref. 71) and $Ln_4Ni_3O_{10-\delta}$ (Ln = La, Pr, Nd).[32] Below, we show that the band scheme in Fig. 9 can also be used to interpret the data of the electrical conductivity of phases $Ln_{n+1}Ni_nO_{3n+1}$, ignoring possible hybridization of the nickel 3d and oxygen 2p orbitals when increasing the formal valence of Ni and the 3D character of the structure of $Ln_{n+1}Ni_nO_{3n+1}$ (*i.e.*, with increasing n), as was suggested by Zhang and Greenblatt.[32]

In accord with the band scheme shown in Fig. 9, the conduction in the RP phases $Ln_{n+1}Ni_nO_{3n+1}$ is metal-like. The $\sigma_{x^2-y^2}\uparrow$ band is completely filled with electrons when the formal valence of Ni is +2 (corresponding to a d^8 configuration). The higher the formal valence of Ni, the lower the Fermi level (E_F), increasing the density of states (DOS) near E_F. Noting that only those electrons in a small energy range near E_F contribute to electrical transport, the electrical conductivity thus increases with an increase in the formal valence of Ni.

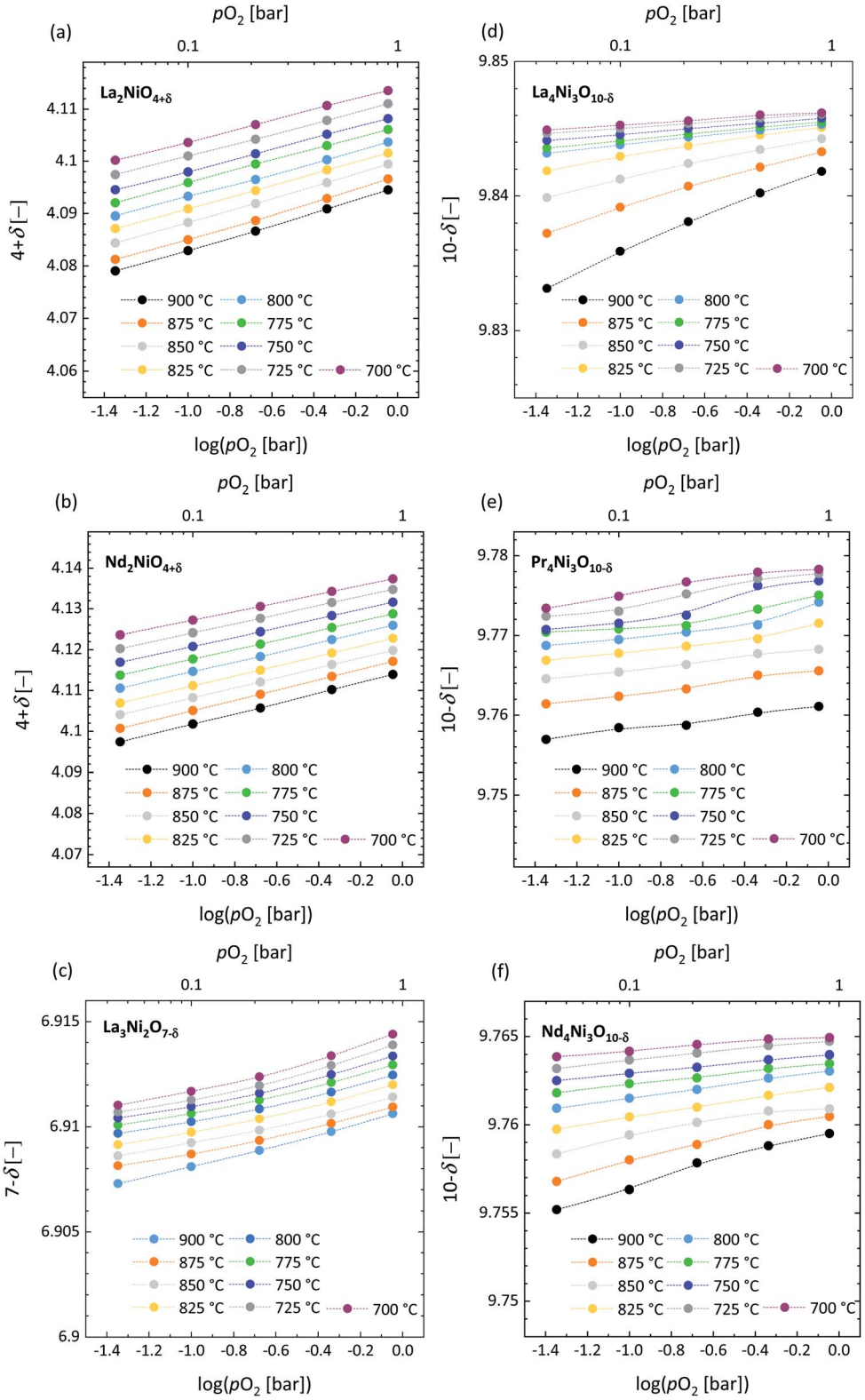

Fig. 7 Oxygen pressure dependence of the oxygen stoichiometry for (a) $La_2NiO_{4+\delta}$, (b) $Nd_2NiO_{4+\delta}$, (c) $La_3Ni_2O_{7-\delta}$, (d) $La_4Ni_3O_{10-\delta}$, (e) $Pr_4Ni_3O_{10-\delta}$, and (f) $Nd_4Ni_3O_{10-\delta}$ at different temperatures. Dotted lines are a guide for the eye.

As an example, under air and in the temperature range 700–900 °C covered by our TGA experiments, the Ni formal valence in phases $La_{n+1}Ni_nO_{3n+1}$ ranges from 2.217 to 2.168 for $n = 1$, from 2.413 to 2.409 for $n = 2$, and from 2.564 to 2.559 for $n = 3$. These results indicate that under the given conditions, the conductivity remains p-type. In accordance with the proposed

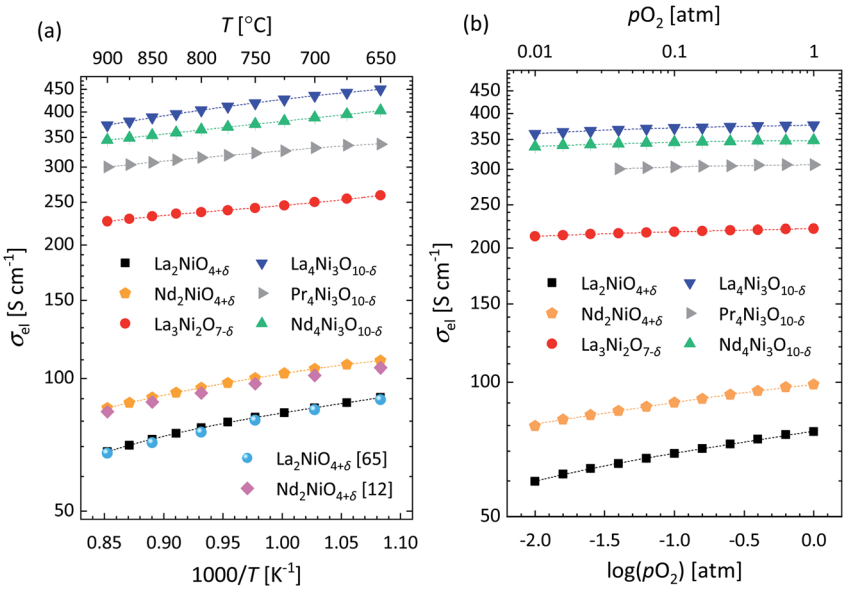

Fig. 8 (a) Inverse temperature dependence, in air, and (b) pO_2 dependence, at 900 °C, of the electrical conductivity (σ_{el}) of $Ln_{n+1}Ni_nO_{3n+1}$ (Ln = La, Pr, Nd; n = 1, 2, 3).* Data for $La_2NiO_{4+\delta}$ and $Nd_2NiO_{4+\delta}$ from the literature are shown for comparison in (a). * Due to instrumental issues, measurements on $Pr_4Ni_3O_{10-\delta}$ were performed over a limited range in pO_2.

band scheme, p-type conductivity persists if there is less than one hole per Ni. Only when the Ni formal valence becomes higher than 3 does the conductivity become n-type (provided that the $\sigma_{x^2-y^2}\uparrow$ does not become fully hybridized with the O-2p band). There are, however, many influences, such as interatomic distances, the presence of lattice defects (*e.g.* oxygen vacancies), disorder (*i.e.*, the range of atomic orbital energies) and inter-electron repulsion, which can cause the electron states to become more localized than the band scheme in Fig. 9 suggests.[72] A more detailed analysis of the electrical conductivity of the RP $Ln_{n+1}Ni_nO_{3n+1}$ nickelates requires data from high temperature Seebeck and Hall coefficient measurements.

3.5 Electrical conductivity relaxation

ECR experiments were conducted for evaluation of the oxygen transport properties of the RP nickelates. Fig. 10 shows the typical normalized conductivity relaxation curves recorded, at 900 °C, after a pO_2 step change from 0.10 atm to 0.21 atm, along with the fitted curves. Note from this figure that slower re-equilibration after the pO_2 step change occurs for the higher order members.

Curve fitting allows simultaneous determination of D_{chem} and k_{chem}, provided that fitting is sensitive to both parameters. As a rule of thumb, though, depending on the accuracy of the

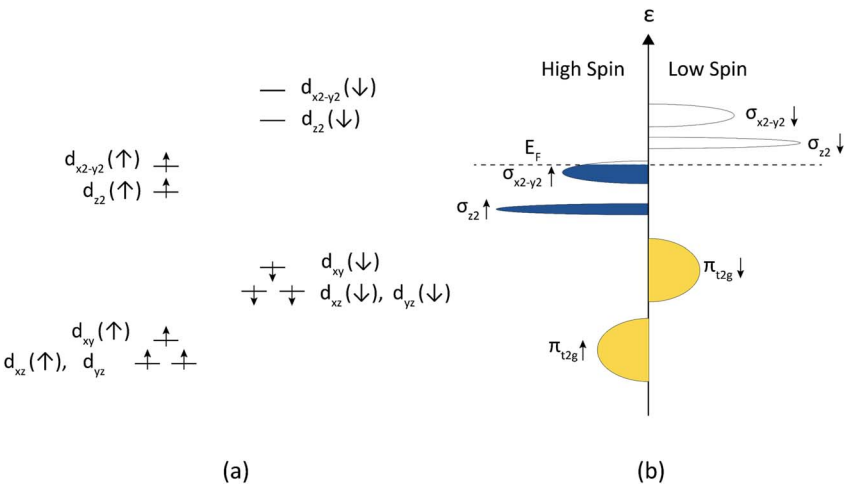

Fig. 9 (a) Crystal field splitting of the bonding Ni 3d orbitals in $Ln_{n+1}Ni_nO_{3n+1}$ and (b) the corresponding schematic density of states (DOS) *vs.* energy diagram. Due to tetragonal distortion of the NiO_6 octahedra, the ε_g ($d_{x^2-y^2}$,d_{z^2}) orbitals are no longer degenerate. Electron–electron correlation leads to further splitting into low and high spin states, while band formation leads to broadening. Note that the Fermi level E_F lowers with the increase of the formal valence of Ni (see the main text).

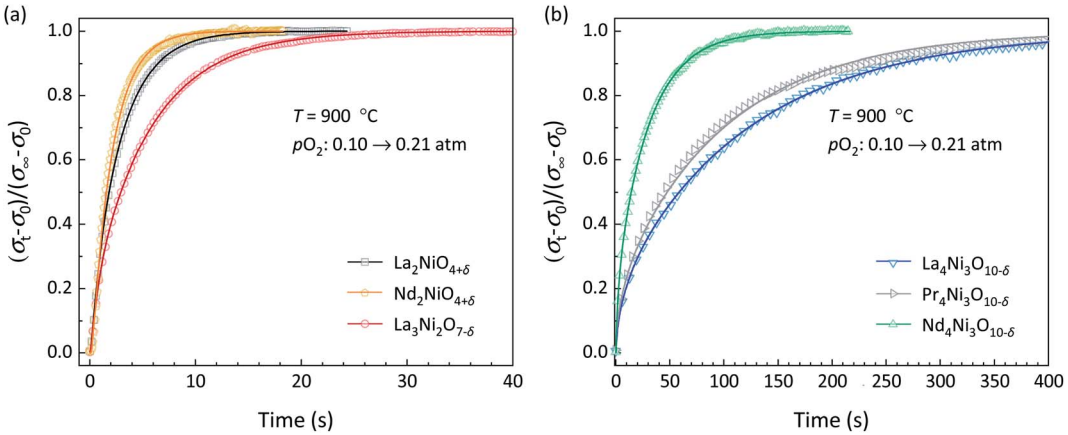

Fig. 10 Typical conductivity relaxation profiles of (a) $La_2NiO_{4+\delta}$, $Nd_2NiO_{4+\delta}$, and $La_3Ni_2O_{7-\delta}$ and (b) $La_4Ni_3O_{10-\delta}$, $Pr_4Ni_3O_{10-\delta}$, and $Nd_4Ni_3O_{10-\delta}$, at 900 °C, after a pO_2 step change from 0.10 atm to 0.21 atm. Full lines represent the corresponding curve fits to eqn (2)–(4).

collected data, both parameters can be reliably assessed if the Biot number (Bi), defined as

$$\mathrm{Bi} = \frac{l_z}{D_{\mathrm{chem}}/k_{\mathrm{chem}}} \quad (7)$$

where l_z is the half-thickness of the sample, lies between 0.03 and 30. Below and above this range, equilibration is predominantly controlled by either surface exchange or diffusion and, hence, fitting becomes rather insensitive to the value of D_{chem} and k_{chem}, respectively.[40]

Fig. 11 shows the temperature dependence of the Biot numbers calculated from the values of D_{chem} and k_{chem} obtained from fitting of the conductivity relaxation curves measured for the different RP nickelates. As seen from this figure, the Biot numbers obtained for the $n = 1$ and $n = 2$ members in the series are in the mixed-controlled region. However, those of the $n = 3$ members are significantly higher than 30, decreasing the accuracy of assessing the values for k_{chem}. The Biot numbers for $Pr_4Ni_3O_{10-\delta}$ could not be calculated as an accurate value of k_{chem} could not be obtained from fitting.

Fig. 12 shows the Arrhenius plots of D_{chem} and k_{chem} of the RP nickelates investigated in this work. In general, fair to good agreement is noted between the values extracted from oxidation and reduction step changes in pO_2. Values for D_{chem} of $La_2NiO_{4+\delta}$ are found to be in good agreement with those reported in the literature.[73] Somewhat surprising at first glance is that the RP nickelates exhibit similar k_{chem} values (Fig. 12c and d), despite the presence of different lanthanide ions, differences in the structural ordering, and, as discussed below, different magnitudes of the oxygen self-diffusion coefficient, and associated ionic conductivity, displayed by the RP phases. Moreover, we examined the SEM images of the samples after completion of the series of ECR experiments (carried out at different temperatures and oxygen partial pressures) and detected significant morphological changes in the surface relative to that of polished samples. As examples, the corresponding SEM images for $La_2NiO_{4+\delta}$, $La_3Ni_2O_{7-\delta}$ and $La_4Ni_3O_{10-\delta}$ are shown in Fig. S16.† The nature and cause of the morphological changes and their possible influence on the apparent surface exchange

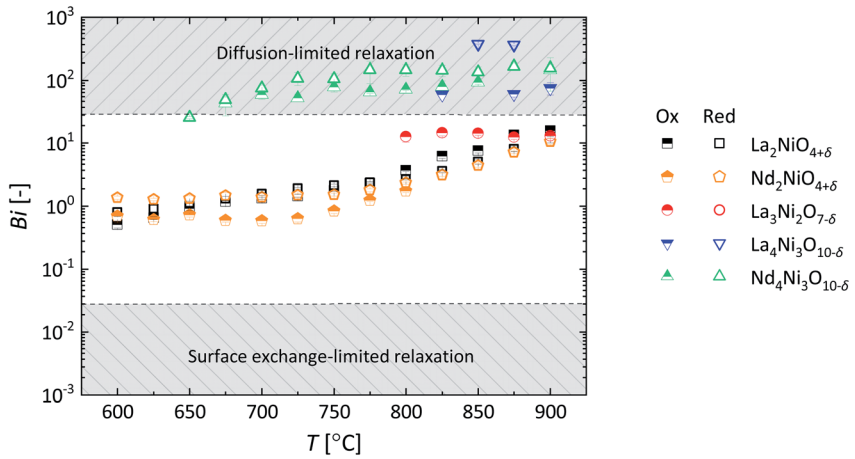

Fig. 11 Temperature dependence of the Biot number (Bi) of materials investigated in this work. As explained in the main text, Biot numbers could not be calculated for $Pr_4Ni_3O_{10-\delta}$.

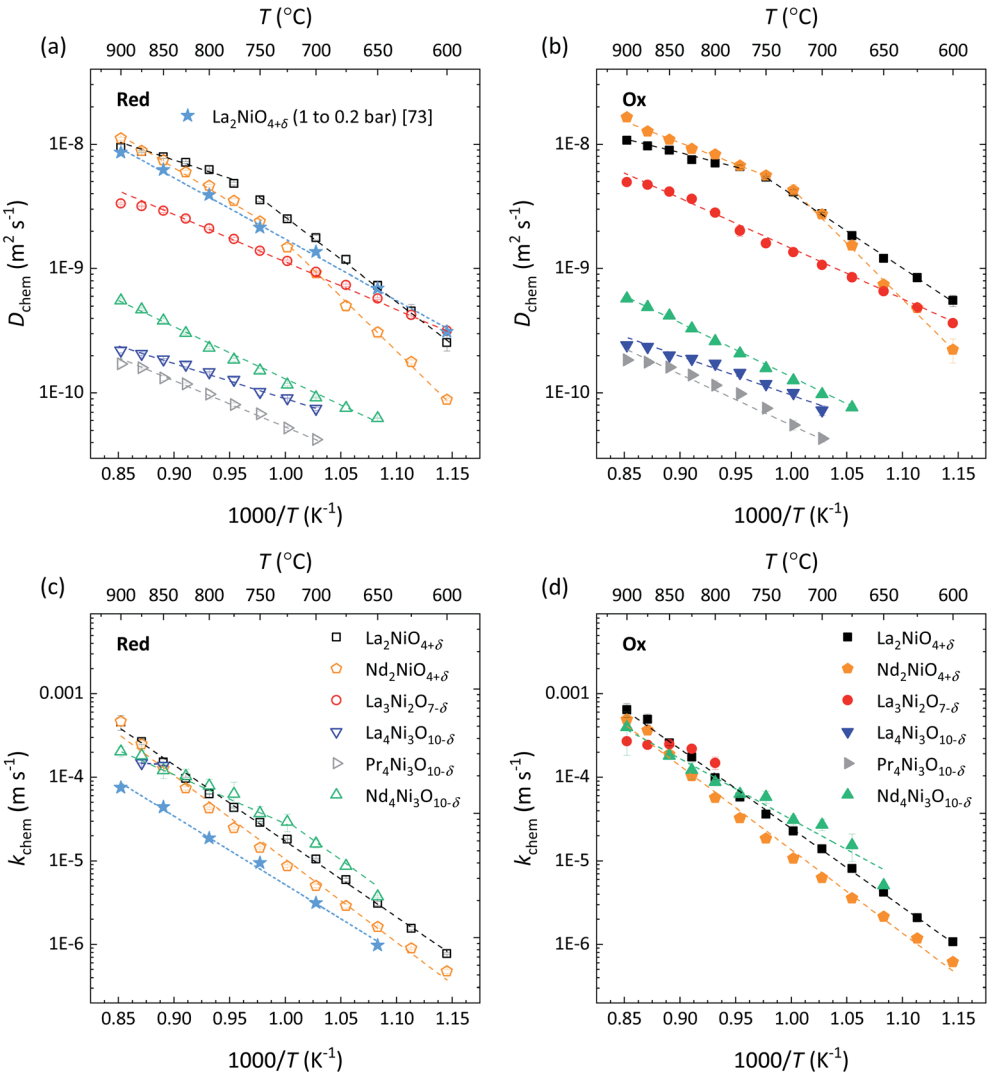

Fig. 12 Arrhenius plots of the (a and b) chemical diffusion coefficient (D_{chem}) and (c and d) surface exchange coefficient (k_{chem}) for $La_2NiO_{4+\delta}$, $Nd_2NiO_{4+\delta}$, $La_3Ni_2O_{7-\delta}$, $La_4Ni_3O_{10-\delta}$, $Pr_4Ni_3O_{10-\delta}$, and $Nd_4Ni_3O_{10-\delta}$. For clarity reasons, data derived from normalized conductivity relaxation curves recorded after oxidation (Ox) and reduction (Red) step changes in pO_2 (between 0.1 and 0.21 atm) are given in separate plots. Error bars are within the symbols. The dashed lines are from linear fitting of the data.

rates of the RP nickelates are currently under investigation in our laboratory.

3.6 Self-diffusion coefficient and ionic conductivity

Apparent oxygen self-diffusion coefficients (D_s) were calculated from the measured values of D_{chem}, using the relationship[39]

$$D_{chem} = \gamma_O D_s \quad (8)$$

where γ_O is the thermodynamic factor. The latter can be calculated from the data of oxygen stoichiometry, using

$$\gamma_O = \frac{1}{2}\frac{\partial \ln(pO_2)}{\partial \ln(c_O)} = \frac{3n+1\pm\delta}{2}\frac{\partial \ln(pO_2)}{\partial(3n+1\pm\delta)} \quad (9)$$

where n is the order of the RP structure and c_O is the oxygen concentration. The inverse temperature dependence of γ_O for each of the RP nickelates investigated in this work as calculated from the data in Fig. 7 is shown in Fig. 13.

The Arrhenius plots of D_s obtained for the different RP nickelates are given in Fig. 14a. Activation energies obtained from least squares fitting of the plots are listed in Table 5. As seen from Fig. 14a, similar values of D_s are found for $La_2NiO_{4+\delta}$ and $Nd_2NiO_{4+\delta}$. Fig. 14b compares these with those derived from the data of tracer diffusion experiments. Ignoring possible correlation factors, good agreement is noted.[9,11] Note further from Fig. 14b that the D_s values obtained for $La_2NiO_{4+\delta}$ and $Nd_2NiO_{4+\delta}$ exceed those measured for $La_{0.6}Sr_{0.4}Co_{0.2}Fe_{0.8}O_{3-\delta}$ (LSCF)[9,74] and $PrBaCo_2O_{5+\delta}$,[75] but are almost one order of magnitude below those reported for $La_{0.3}Sr_{0.7}CoO_{3-\delta}$.[76] Ionic conductivities of the RP nickelates calculated from the apparent values of D_s (Fig. 14a) using the Nernst–Einstein equation are shown in Fig. 15.

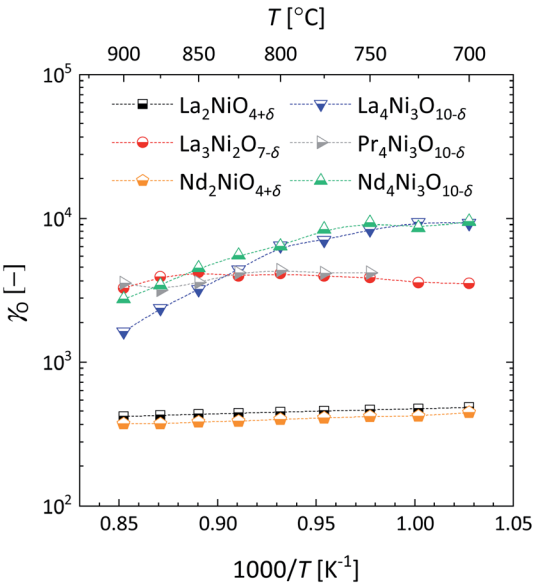

Fig. 13 Reciprocal temperature dependence of the thermodynamic factor of oxygen (γ_O), at $pO_2 = 0.1468$ atm, for different RP nickelates. The cited pO_2 value corresponds to the logarithmic average of the initial and final pO_2 used in ECR measurements.

Most notable from Fig. 14a is the sequence of the magnitude of D_s observed for the $n = 1$, $n = 2$ and $n = 3$ members of the RP nickelates, differing by almost one order of magnitude from each other. The highest values are found for $Ln_{n+1}Ni_nO_{3n+1}$ with Ln = La, Nd and $n = 1$ and the lowest are found for Ln = La, Pr, Nd and $n = 3$. To account for this observation, it is recalled that

Table 5 Activation energies (E_a) of D_s for different RP nickelates and the corresponding correlations of determination (R^2) from linear regression analysis. The values of D_s were taken from Fig. 14a

Materials	E_a (eV)	R^2 (—)
$La_2NiO_{4+\delta}$	0.65 ± 0.05	0.95
$Nd_2NiO_{4+\delta}$	0.88 ± 0.04	0.98
$La_3Ni_2O_{7-\delta}$	0.80 ± 0.03	0.98
$La_4Ni_3O_{10-\delta}$	1.44 ± 0.07	0.98
$Pr_4Ni_3O_{10-\delta}$	0.91 ± 0.08	0.95
$Nd_4Ni_3O_{10-\delta}$	1.51 ± 0.07	0.98

oxygen migration in the RP structures is believed to occur in the rock salt layers *via* a cooperative interstitialcy mechanism.[14,17–19,77–81] The apparent value of D_s reflects an ensemble property, being averaged over all oxygen ions (interstitial, apical and equatorial) in the lattice. As alluded to before, oxygen hyper-stoichiometry ($\delta > 0$) is found for the $n = 1$ RP nickelates, which is accommodated by oxygen interstitials in the rock salt layers. Higher concentrations of oxygen interstitials will lead to higher values for D_s and the associated ionic conductivity (σ_{ion}). The $n = 2$ and $n = 3$ RP nickelates, on the other hand, exhibit oxygen hypo-stoichiometries ($\delta < 0$). The intrinsic disorder in the RP nickelates is known to be of the anti-Frenkel type, with oxygen vacancies preferably residing on equatorial sites.[14,82–84] Due to the oxygen hypo-stoichiometry, the concentration of oxygen interstitials in the $n = 2$ RP nickelates is expected to be small. Compared to these, the $n = 3$ members exhibit even higher oxygen hypo-stoichiometries, further reducing the concentration of oxygen interstitials in the rock-salt layers and,

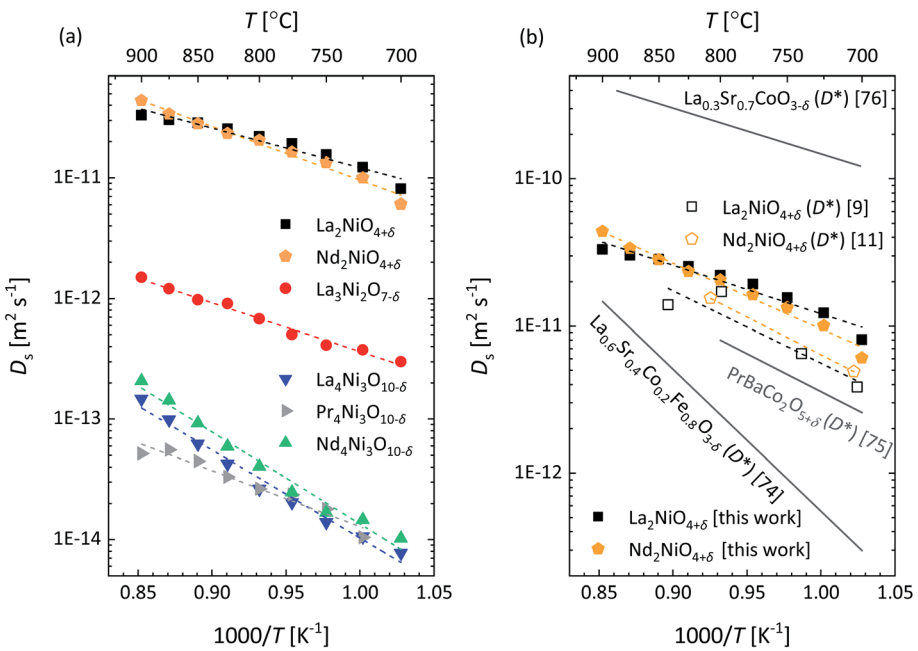

Fig. 14 (a) Arrhenius plots of the oxygen self-diffusion coefficient (D_s) of RP nickelates investigated in this work and (b) comparison of D_s measured for $La_2NiO_{4+\delta}$ and $Nd_2NiO_{4+\delta}$ with the tracer diffusion coefficient (D^*) of selected perovskite oxides reported in the literature. For clarity reasons, only values of D_s (this work) derived from normalized conductivity relaxation curves recorded after oxidation step changes in pO_2 (from 0.1 atm to 0.21 atm) are shown.

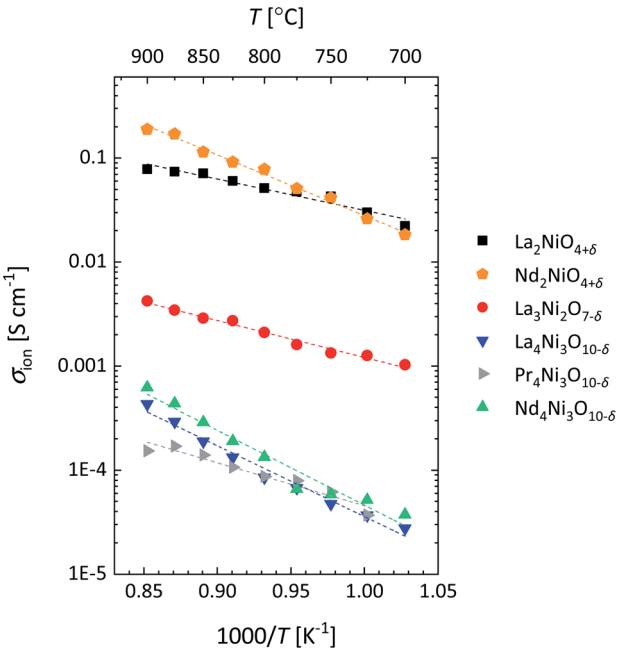

Fig. 15 Arrhenius plots of the ionic conductivity (σ_{ion}) of RP nickelates investigated in this work. Ionic conductivities were calculated from the values of D_s (Fig. 14a) using the Nernst–Einstein equation.

hence, the values for D_s and σ_{ion}. It should be noted that the above analysis ignores that (impurities near) grain boundaries and differences in the spatial distributions of grain orientation and grain size in the polycrystalline samples may exert an influence on the apparent values of D_s and σ_{ion}.

In a molecular dynamics study of oxygen migration in the acceptor-doped system $La_{2-x}Sr_xCoO_{4\pm\delta}$ ($x > 0.8$), Tealdi *et al.*[80] confirmed that oxygen transport in hyper-stoichiometric $La_{0.8}Sr_{1.2}CoO_{4.1}$ is *via* an interstitialcy mechanism in the rock salt layer, but that in hypo-stoichiometric $La_{0.8}Sr_{1.2}CoO_{3.9}$ mainly occurs through the migration of oxygen vacancies within the perovskite layer of the structure. Manthiram *et al.*[85] suggested that oxygen vacancies dominate oxygen transport in the higher order RP phases $La_{0.3}Sr_{2.7}CoFeO_{7-\delta}$ ($n = 2$) and $LaSr_3Co_{1.5}Fe_{1.5}O_{10-\delta}$ ($n = 3$), showing about one order of magnitude higher oxygen permeation fluxes than the $n = 1$ members $La_{0.8}Sr_{1.2}CoO_{4+\delta}$ and $La_{0.8}Sr_{1.2}FeO_{4+\delta}$. The results of this study give firm evidence that oxygen migrates predominantly *via* an interstitialcy mechanism in the undoped RP nickelates $Ln_{n+1}Ni_nO_{3n+1}$ (Ln = La, Pr and Nd; $n = 1$, 2 and 3), hence implicitly suggesting a negligible role of oxygen vacancies in determining oxygen transport in the $n = 2$ and $n = 3$ members despite their oxygen hypo-stoichiometries (*cf.* Fig. 7). Finally, it is difficult to account for the lower activation energy of oxygen migration in $Pr_4Ni_3O_{10-\delta}$ compared with the corresponding values found for $La_4Ni_3O_{10-\delta}$ and $Nd_4Ni_3O_{10-\delta}$ (*cf.* Table 5). It is hypothesized to arise from concomitant Pr valence and, hence, size changes (due to significant Pr 4f and O 2p orbital hybridization) upon oxygen migration in $Pr_4Ni_3O_{10-\delta}$.[86] First-principles density functional theory calculations are required to support this hypothesis.

4. Conclusions

In this work, the thermal evolution of the structure, oxygen nonstoichiometry, electrical conductivity and oxygen transport properties of Ruddlesden–Popper (RP) lanthanide nickelates $Ln_{n+1}Ni_nO_{3n+1}$ (Ln = La, Pr and Nd; $n = 1$, 2 and 3) have been investigated. The compositions $Pr_2NiO_{4+\delta}$, $Pr_3Ni_2O_{7-\delta}$ and $Nd_3Ni_2O_{7-\delta}$ have been excluded from this work because the material either cannot be prepared in a phase pure form ($Pr_3Ni_2O_{7-\delta}$ and $Nd_3Ni_2O_{7-\delta}$) or fully decomposes at moderate temperatures ($Pr_2NiO_{4+\delta}$). Upon heating in air phase transitions, involving changes in the tilting of the NiO_6 octahedra, are observed in several of the materials. $Pr_4Ni_3O_{10-\delta}$ and $Nd_4Ni_3O_{10-\delta}$ remain monoclinic from room temperature up to 1000 °C, showing no observable phase transition.

High density ceramic samples were obtained by sintering at 1300 °C and, for the $n = 2$ and $n = 3$ members, post-sintering annealing at reduced temperatures. The results of electrical conductivity measurements on these samples support the itinerant behaviour of the charge carriers in the RP nickelates. The increase in the p-type conductivity of the RP phases with the order parameter n can be interpreted in terms of a simple energy band scheme, showing that electron holes are formed in the $\sigma_{x^2-y^2}\uparrow$ band upon increasing the oxidation state of Ni.

The RP nickelates display remarkable similarity in their values for the surface exchange coefficient (k_{chem}) despite the differences in the structure and the type of lanthanide ion. The oxygen self-diffusion coefficients (D_s) calculated from the corresponding values of the chemical diffusion coefficient (D_{chem}), using the data of oxygen non-stoichiometry, are found to decrease profoundly with the order parameter n. While oxygen hyper-stoichiometry ($\delta > 0$) is found in the $n = 1$ compositions, oxygen hypo-stoichiometry ($\delta < 0$) is found in the $n = 2$ and $n = 3$ compositions. The results of this study underpin that oxygen transport in the undoped RP nickelates mainly occurs *via* an interstitialcy mechanism within the rock-salt layer of the structures.

Conflicts of interest

There are no conflicts to declare.

Acknowledgements

Financial support from the Dutch Technology Foundation (STW, now part of NWO; Project Nr. 15325) and the Chinese Scholarship Council (CSC 201406340102) are gratefully acknowledged.

References

1 G. Amow and S. J. Skinner, *J. Solid State Electrochem.*, 2006, **10**, 538–546.
2 A. Tarancón, M. Burriel, J. Santiso, S. J. Skinner and J. A. Kilner, *J. Mater. Chem.*, 2010, **20**, 3799–3813.
3 R. K. Sharma, M. Burriel, L. Dessemond, J.-M. Bassat and E. Djurado, *J. Power Sources*, 2016, **325**, 337–345.

4 V. Vibhu, A. Rougier, C. Nicollet, A. Flura, S. Fourcade, N. Penin, J.-C. Grenier and J.-M. Bassat, *J. Power Sources*, 2016, **317**, 184–193.
5 M. A. Yatoo, Z. Du, H. Zhao, A. Aguadero and S. J. Skinner, *Solid State Ionics*, 2018, **320**, 148–151.
6 M. A. Yatoo, A. Aguadero and S. J. Skinner, *APL Mater.*, 2019, **7**, 013204.
7 F. Grimm, N. H. Menzler, P. Lupetin and O. Guillon, *ECS Trans.*, 2019, **91**, 1397.
8 M. T. Fernández-Díaz, J. L. Martínez and J. Rodríguez-Carvajal, *Solid State Ionics*, 1993, **63**, 902–906.
9 S. Skinner and J. Kilner, *Solid State Ionics*, 2000, **135**, 709–712.
10 S. J. Skinner, *Solid State Sci.*, 2003, **5**, 419–426.
11 E. Boehm, J. Bassat, P. Dordor, F. Mauvy, J. Grenier and P. Stevens, *Solid State Ionics*, 2005, **176**, 2717–2725.
12 T. Nakamura, K. Yashiro, K. Sato and J. Mizusaki, *Mater. Chem. Phys.*, 2010, **122**, 250–258.
13 S. Takahashi, S. Nishimoto, M. Matsuda and M. Miyake, *J. Am. Ceram. Soc.*, 2010, **93**, 2329–2333.
14 L. Minervini, R. W. Grimes, J. A. Kilner and K. E. Sickafus, *J. Mater. Chem.*, 2000, **10**, 2349–2354.
15 J.-M. Bassat, *Solid State Ionics*, 2004, **167**, 341–347.
16 J.-M. Bassat, M. Burriel, M. Ceretti, P. Veber, J.-C. Grenier, W. Paulus and J. A. Kilner, *ECS Trans.*, 2013, **57**, 1753–1760.
17 D. Lee and H. N. Lee, *Materials*, 2017, **10**, 368.
18 M. Yashima, M. Enoki, T. Wakita, R. Ali, Y. Matsushita, F. Izumi and T. Ishihara, *J. Am. Chem. Soc.*, 2008, **130**, 2762–2763.
19 A. Chroneos, D. Parfitt, J. A. Kilner and R. W. Grimes, *J. Mater. Chem.*, 2010, **20**, 266–270.
20 A. Flura, S. Dru, C. Nicollet, V. Vibhu, S. Fourcade, E. Lebraud, A. Rougier, J.-M. Bassat and J.-C. Grenier, *J. Solid State Chem.*, 2015, **228**, 189–198.
21 M. J. Escudero, A. Fuerte and L. Daza, *J. Power Sources*, 2011, **196**, 7245–7250.
22 E. Dogdibegovic, W. Guan, J. Yan, M. Cheng and X.-D. Zhou, *J. Electrochem. Soc.*, 2016, **163**, F1344–F1349.
23 S. Saher, J. Song, V. Vibhu, C. Nicollet, A. Flura, J.-M. Bassat and H. J. M. Bouwmeester, *J. Mater. Chem. A*, 2018, **6**, 8331–8339.
24 D. Ning, A. Baki, T. Scherb, J. Song, A. Fantin, X. Liu, G. Schumacher, J. Banhart and H. J. M. Bouwmeester, *Solid State Ionics*, 2019, **342**, 115056.
25 V. Vibhu, J.-M. Bassat, A. Flura, C. Nicollet, J.-C. Grenier and A. Rougier, *ECS Trans.*, 2015, **68**, 825–835.
26 J.-M. Bassat, V. Vibhu, C. Nicollet, A. Flura, S. Fourcade, J.-C. Grenier and A. Rougier, *ECS Trans.*, 2017, **78**, 655–665.
27 T. Broux, C. Prestipino, M. Bahout, S. Paofai, E. Elkaim, V. Vibhu, J. C. Grenier, A. Rougier, J. M. Bassat and O. Hernandez, *Dalton Trans.*, 2016, **45**, 3024–3033.
28 J. Sullivan, D. Buttrey, D. Cox and J. Hriljac, *J. Solid State Chem.*, 1991, **94**, 337–351.
29 E. Pikalova, A. Kolchugin, N. Bogdanovich, D. Medvedev, J. Lyagaeva, L. Vedmid, M. Ananyev, S. Plaksin and A. Farlenkov, *Int. J. Hydrogen Energy*, 2020, **45**, 13612–13624.
30 P. Odier, C. Allançon and J. M. Bassat, *J. Solid State Chem.*, 2000, **153**, 381–385.
31 A. Egger, *Rare Earth Nickelates as Cathodes for Solid Oxide Fuel Cells*, PhD thesis, Montanuniversität Leoben, Leoben, Austria, 2013.
32 Z. Zhang and M. Greenblatt, *J. Solid State Chem.*, 1995, **117**, 236–246.
33 G. Amow, I. Davidson and S. Skinner, *Solid State Ionics*, 2006, **177**, 1205–1210.
34 R. J. Woolley and S. J. Skinner, *J. Power Sources*, 2013, **243**, 790–795.
35 D. O. Bannikov and V. A. Cherepanov, *J. Solid State Chem.*, 2006, **179**, 2721–2727.
36 R. K. Sharma, M. Burriel and E. Djurado, *J. Mater. Chem. A*, 2015, **3**, 23833–23843.
37 S. F. P. ten Donkelaar, R. Ruhl, S. A. Veldhuis, A. Nijmeijer, L. Winnubst and H. J. M. Bouwmeester, *Ceram. Int.*, 2015, **41**, 13709–13715.
38 J. Rodriguezcarvajal, *Phys. B*, 1993, **192**, 55–69.
39 J. E. ten Elshof, M. H. R. Lankhorst and H. J. M. Bouwmeester, *J. Electrochem. Soc.*, 1997, **144**, 1060–1067.
40 M. W. den Otter, H. J. M. Bouwmeester, B. A. Boukamp and H. Verweij, *J. Electrochem. Soc.*, 2001, **148**, J1.
41 A. Olafsen, H. Fjellvåg and B. C. Hauback, *J. Solid State Chem.*, 2000, **151**, 46–55.
42 M. Zinkevich and F. Aldinger, *J. Alloys Compd.*, 2004, **375**, 147–161.
43 M. U. Nagell, W. A. Sławiński, P. Vajeeston, H. Fjellvåg and A. O. Sjåstad, *Solid State Ionics*, 2017, **305**, 7–15.
44 M. Ceretti, O. Wahyudi, G. Andre, M. Meven, A. Villesuzanne and W. Paulus, *Inorg. Chem.*, 2018, **57**, 4657–4666.
45 V. Vibhu, M. R. Suchomel, N. Penin, F. Weill, J. C. Grenier, J. M. Bassat and A. Rougier, *Dalton Trans.*, 2018, **48**, 266–277.
46 E. A. Kiselev, P. Gaczynski, G. Eckold, A. Feldhoff, K. D. Becker and V. A. Cherepanov, *Chim. Techno Acta*, 2019, **6**, 51–71.
47 J. Zhang, H. Zheng, Y. S. Chen, Y. Ren, M. Yonemura, A. Huq and J. F. Mitchell, 2019, arXiv:1904.10048.
48 R. D. Shannon, *Acta Crystallogr., Sect. A: Cryst. Phys., Diffr., Theor. Gen. Crystallogr.*, 1976, **32**, 751–767.
49 D. Guan, J. Zhou, Y. C. Huang, C. L. Dong, J. Q. Wang, W. Zhou and Z. Shao, *Nat. Commun.*, 2019, **10**, 3755.
50 D. M. Halat, R. Dervişoğlu, G. Kim, M. T. Dunstan, F. D. R. Blanc, D. S. Middlemiss and C. P. Grey, *J. Am. Chem. Soc.*, 2016, **138**, 11958–11969.
51 T. Nakamura, K. Yashiro, K. Sato and J. Mizusaki, *Solid State Ionics*, 2010, **181**, 402–411.
52 Y. Toyosumi, H. Ishikawa and K. Ishikawa, *J. Alloys Compd.*, 2006, **408–412**, 1200–1204.
53 A. Aguadero, J. A. Alonso, M. J. Martínez-Lope, M. T. Fernández-Díaz, M. J. Escudero and L. Daza, *J. Mater. Chem.*, 2006, **16**, 3402–3408.
54 M. Nagamori, T. Shimonosono, S. Sameshima, Y. Hirata, N. Matsunaga and Y. Sakka, *J. Am. Ceram. Soc.*, 2009, **92**, S117–S121.

55 M. Rotan, J. Tolchard, E. Rytter, M.-A. Einarsrud and T. Grande, *J. Solid State Chem.*, 2009, **182**, 3412–3415.
56 O. Wahyudi, M. Ceretti, I. Weill, A. Cousson, F. Weill, M. Meven, M. Guerre, A. Villesuzanne, J. M. Bassat and W. Paulus, *CrystEngComm*, 2015, **17**, 6278–6285.
57 R. Retoux, J. Rodriguez-Carvajal and P. Lacorre, *J. Solid State Chem.*, 1998, **140**, 307–315.
58 J. Kilner and C. Shaw, *Solid State Ionics*, 2002, **154**, 523–527.
59 J. Zhang, A. S. Botana, J. W. Freeland, D. Phelan, H. Zheng, V. Pardo, M. R. Norman and J. F. Mitchell, *Nat. Phys.*, 2017, **13**, 864–869.
60 R. J. Woolley, B. N. Illy, M. P. Ryan and S. J. Skinner, *J. Mater. Chem.*, 2011, **21**, 18592–18596.
61 E. N. Naumovich, M. V. Patrakeev, V. V. Kharton, A. A. Yaremchenko, D. I. Logvinovich and F. M. B. Marques, *Solid State Sci.*, 2005, **7**, 1353–1362.
62 T. Nakamura, K. Yashiro, K. Sato and J. Mizusaki, *J. Solid State Chem.*, 2009, **182**, 1533–1537.
63 D.-P. Huang, Q. Xu, F. Zhang, W. Chen, H.-x. Liu and J. Zhou, *Mater. Lett.*, 2006, **60**, 1892–1895.
64 Z. Lou, J. Peng, N. Dai, J. Qiao, Y. Yan, Z. Wang, J. Wang and K. Sun, *Electrochem. Commun.*, 2012, **22**, 97–100.
65 Z. Lou, N. Dai, Z. Wang, Y. Dai, Y. Yan, J. Qiao, J. Peng, J. Wang and K. Sun, *J. Solid State Electrochem.*, 2013, **17**, 2703–2709.
66 T. Nakamura, K. Yashiro, K. Sato and J. Mizusaki, *Phys. Chem. Chem. Phys.*, 2009, **11**, 3055–3062.
67 J. Bassat, P. Odier and J. Loup, *J. Solid State Chem.*, 1994, **110**, 124–135.
68 S. Nishiyama, D. Sakaguchi and T. Hattori, *Solid State Commun.*, 1995, **94**, 279–282.
69 J. B. Goodenough, *Mater. Res. Bull.*, 1973, **8**, 423–431.
70 J. B. Goodenough and S. Ramasesha, *Mater. Res. Bull.*, 1982, **17**, 383–390.
71 Z. Zhang, M. Greenblatt and J. Goodenough, *J. Solid State Chem.*, 1994, **108**, 402–409.
72 P. A. Cox, in *Physics and Chemistry of Low-Dimensional Inorganic Conductors*, Springer, 1996, pp. 255–270.
73 Z. Li and R. Haugsrud, *Solid State Ionics*, 2012, **206**, 67–71.
74 S. Benson, D. Waller and J. Kilner, *J. Electrochem. Soc.*, 1999, **146**, 1305–1309.
75 M. Burriel, J. Peña-Martínez, R. J. Chater, S. Fearn, A. V. Berenov, S. J. Skinner and J. A. Kilner, *Chem. Mater.*, 2012, **24**, 613–621.
76 R. E. van Doorn, I. C. Fullarton, R. A. de Souza, J. A. Kilner, H. J. M. Bouwmeester and A. J. Burggraaf, *Solid State Ionics*, 1997, **96**, 1–7.
77 M. Yashima, N. Sirikanda and T. Ishihara, *J. Am. Chem. Soc.*, 2010, **132**, 2385–2392.
78 A. Chroneos, D. Parfitt, R. V. Vovk and I. L. Goulatis, *Mod. Phys. Lett. B*, 2012, **26**, 1250196.
79 D. Parfitt, A. Chroneos, J. A. Kilner and R. W. Grimes, *Phys. Chem. Chem. Phys.*, 2010, **12**, 6834–6836.
80 C. Tealdi, C. Ferrara, P. Mustarelli and M. S. Islam, *J. Mater. Chem.*, 2012, **22**, 8969–8975.
81 A. Kushima, D. Parfitt, A. Chroneos, B. Yildiz, J. A. Kilner and R. W. Grimes, *Phys. Chem. Chem. Phys.*, 2011, **13**, 2242–2249.
82 C. Frayret, A. Villesuzanne and M. Pouchard, *Chem. Mater.*, 2005, **17**, 6538–6544.
83 A. Cleave, J. Kilner, S. Skinner, S. Murphy and R. Grimes, *Solid State Ionics*, 2008, **179**, 823–826.
84 A. C. Tomkiewicz, M. Tamimi, A. Huq and S. McIntosh, *J. Mater. Chem. A*, 2015, **3**, 21864–21874.
85 A. Manthiram, F. Prado and T. Armstrong, *Solid State Ionics*, 2002, **152**, 647–655.
86 J. Herrero-Martín, J. García-Muñoz, S. Valencia, C. Frontera, J. Blasco, A. Barón-González, G. Subías, R. Abrudan, F. Radu and E. Dudzik, *Phys. Rev. B*, 2011, **84**, 115131.